CFD analysis of microchannel emulsification: droplet generation process and size effect of asymmetric straight flow-through microchannels

Isao Kobayashi[a,*], Goran T. Vladisavljević[b], Kunihiko Uemura[a], and Mitsutoshi Nakajima[a,c,**]

[a] *Food Engineering Division, National Food Research Institute, NARO,*

2-1-12 Kannondai, Tsukuba, Ibaraki 305-8642, Japan

[b] *Chemical Engineering Department, Loughborough University, Loughborough,*

Leicestershire, LE11 3TU, UK

[c] *Graduate School of Life and Environmental Sciences, University of Tsukuba, 1-1-1*

Tennoudai, Tsukuba, Ibaraki 305-8572, Japan

*Tel: +81-29-838-8025, Fax: +81-29-838-8122, E-mail: isaok@affrc.go.jp

** Tel: +81-29-853-3981, Fax: +81-29-853-4703, E-mail: mnaka@sakura.cc.tsukuba.ac.jp

Abstract:

Asymmetric straight flow-through microchannel (MC) arrays are high-performance MC emulsification devices for stable mass production of uniform droplets. This paper presents computational fluid dynamics (CFD) simulation and analysis of the generation of soybean oil-in-water emulsion droplets via asymmetric straight flow-through MCs, each consisting of a microslot and a narrow MC. We also used CFD to investigate the effects of the channel size and the flow of the dispersed phase on MC emulsification using asymmetric straight flow-through MCs with a characteristic channel size of 5 to 400 μm. The overall shape of an oil-water interface and the time scale during droplet generation via a control asymmetric straight flow-through MC were appropriately simulated. Better insight was obtained on the flow profile of the two phases and the internal pressure balance of the dispersed phase during droplet generation. Comparison of the CFD and experiment results also provided insight into dynamic interfacial tension during droplet generation. Successful droplet generation was observed below a critical dispersed-phase velocity. In this case, the resultant droplet size was proportional to the channel size and was not sensitive to the dispersed-phase velocity applied. The maximum droplet generation rate per channel was inversely proportional to the channel size, unless the buoyancy force did not promote droplet detachment. The maximum droplet productivity per unit area of an asymmetric straight flow-through MC array was estimated to be constant, regardless of channel size.

Key words: Microchannel emulsification, CFD, simulation, channel size, droplet productivity

1. Introduction

Emulsification techniques using microfluidic devices have recently received a great deal of attention in various fields (e.g., foods, pharmaceuticals, biomedicals, cosmetics, and chemicals). Advantages of these microfluidic emulsification techniques include the generation of uniform droplets, the precise control of droplet size and droplet shape, and *in situ* microscopic monitoring that allows fine tuning of the process parameters during droplet generation. In addition, the size uniformity of emulsion droplets is required for making monodisperse dispersions containing microparticles (Sugiura et al. 2001a; Xu et al. 2005), microcapsules (Nakagawa et al. 2004; Utada et al. 2005; Seiffert et al. 2010), or other new classes of micromaterials (Yi et al. 2003; Nie et al. 2006; Nishisako and Torii 2007; Sugiura et al. 2008). Traditional emulsification devices (e.g., colloid mills, high-pressure valve homogenizers, and ultrasonic homogenizers) use intensive force to repeatedly break up larger droplets into smaller ones (McClements 2004). The emulsions produced using these devices usually have wide droplet size distributions, and their droplet size is empirically adjusted.

Microfluidic droplet-generation devices consisting of an interconnected channel configuration have been developed within the last decade (Günther and Jensen 2006). The most commonly used microfluidic channel configurations are T-junction (Thorsen et al. 2001; Nishisako et al. 2002; Xu et al. 2006) and flow-focusing (Anna et al. 2003; Xu and Nakajima 2004; Yobas et al. 2006). Droplet generation in a T-junction requires the crossflow of the continuous phase (Garstecki et al. 2006), and flow-focusing configurations are driven by the coflow of the continuous phase (Abate et al. 2009). Uniform droplets can be generated using these microfluidic droplet-generation devices, whereas the size of the generated droplets is greatly influenced by the flow rate of both phases. A few research groups have recently developed microfluidic devices consisting of parallelized cross-junction or flow-focusing configurations to increase droplet productivity (Nishisako and Torii 2008; Tetradis-Meris et al.

2009; Li et al. 2009). However, successful droplet generation over a long period is difficult, since the flow rate of both phases must be equally controlled at all droplet generation units. Computational fluid dynamics (CFD) methods have also been used to simulate and analyze droplet generation in microfluidic channel configurations (Sang et al. 2008; Kashid et al. 2010; Zhou et al. 2006; de Menech et al. 2008; Gupta and Kumar 2010).

Microchannel (MC) emulsification, proposed by Kawakatsu et al. (1997), is another microfluidic droplet-generation technique. MC emulsification devices are composed of many grooved MCs with a slit-like terrace (Kawakatsu et al. 1999) or many straight flow-through MCs (Kobayashi et al. 2002a). Droplet generation for MC emulsification is a unique and robust process driven by spontaneous transformation of the dispersed phase that passes through channels (Sugiura et al. 2001b). This geometry-dominated droplet generation occurs in the absence of the external flow of a continuous phase. MC emulsification devices can generate uniform droplets of 1 to 180 μm (Kobayashi et al. 2007; 2010). The resultant droplet size is primarily determined by the dimensions of the MC array (Sugiura et al. 2002a). The droplet size and its distribution are barely influenced by the velocity of each phase below a critical value (Sugiura et al. 2002b; Kobayashi et al. 2003), indicating that MC emulsification is useful for practical production of monodisperse emulsions. Moreover, straight flow-through MC arrays are promising for mass production of uniform droplets, since numerous channels (e.g., 10^4 cm^{-2}) can be compactly arranged on an MC emulsification device (Kobayashi et al. 2002a; 2005a).

Only a few research groups have studied droplet generation by MC emulsification using CFD methods. Kobayashi et al. (2004; 2005b; 2006) simulated droplet generation from symmetric straight flow-through MCs using a CFD package (CDF-ACE+) employing a finite volume method. The authors gained important insight into the movement of an oil-water interface and the flow and pressure fields during droplet generation from straight

flow-through MCs with different cross-sectional shapes. Kobayashi et al. (2005b; 2006) also demonstrated that the CFD method can appropriately simulate the effects of dispersed-phase viscosity and dispersed-phase velocity as dynamic operation parameters. Van Dijke et al. (2008) and van der Zwan et al. (2009) modeled droplet generation from a grooved MC using a finite volume method (Star-CD) and a lattice Boltzmann method, respectively. Rayner et al. (2004) also used an interactive program (Surface Evolver) to simulate the droplet size for straight flow-through MC emulsification. This program computes the interfacial shape with the minimum free energy in the state of equilibrium. Although simulations using the Surface Evolver can estimate the largest stable volume of a droplet attached to the channel outlet, the effects of dynamic operation parameters cannot be determined.

Kobayashi et al. (2005a) developed asymmetric straight flow-through MCs, each consisting of a microslot and a circular MC (Fig. 1). Asymmetric straight flow-through MC arrays produced monodisperse emulsions at a dispersed-phase flux (i.e., droplet productivity) exceeding those of the other types of MC arrays (Vladisavljević et al. 2006). Asymmetric straight flow-through MCs also enable the stable generation of uniform droplets of low-viscosity oil (Kobayashi et al. 2005a), which differs from droplet generation using symmetric straight flow-through MCs. Hence, asymmetric straight flow-through MC arrays are recognized as high-performance MC emulsification devices. The current asymmetric straight flow-through MC arrays can produce monodisperse emulsions with a droplet size of 30 to 180 μm (Kobayashi et al. 2005a; 2010a), whereas scaling laws for asymmetric straight flow-through MCs are not yet clear. In addition, with optical microscopy it is greatly difficult to observe the movement of the oil-water interface in asymmetric straight flow-through MCs during droplet generation, because the interior of the channel is not optically accessible (Fig. 1b). The use of CFD is expected to provide useful insight into these problems; however, CFD has not yet been used to simulate droplet generation from asymmetric straight flow-through

MCs.

In this study, we have systematically investigated droplet generation from asymmetric straight flow-through MCs using CFD. We have simulated the droplet generation process for a control asymmetric straight flow-through MC and analyzed interfacial tension and flow and pressure profiles during droplet generation. We also investigated the effects of channel size and flow rate of the dispersed phase on MC emulsification using asymmetric straight flow-through MCs.

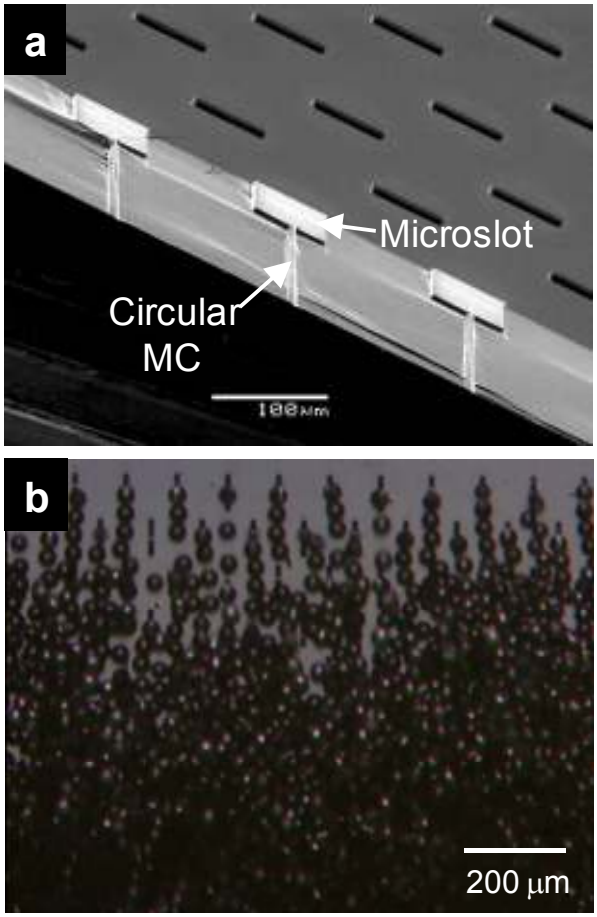

Fig. 1 MC emulsification using asymmetric straight flow-through MCs (Kobayashi et al. 2010b). (a) Scanning electron micrograph of asymmetric straight flow-through MCs microfabricated within a 10×10 mm central region on a 24×24 mm silicon-on-insulator chip. (b) Example of the mass production of uniform soybean oil droplets from the slot outlets at a dispersed-phase flux of 100 L m^{-2} h^{-1}. A Milli-Q water solution containing 0.3 wt% sodium dodecyl sulfate was used as the continuous phase.

2. Materials and methods

2.1. Problem description and computational domain

We investigated emulsion droplet generation from asymmetric straight flow-through MCs, each consisting of a microslot and a narrow MC. The 3D transient droplet generation via an asymmetric straight flow-through MC was modeled using a general purpose CFD software package, *CFD-ACE+*. A domain for emulsion droplet generation that includes an asymmetric straight flow-through MC is depicted in Fig. 2. A dispersed oil phase is injected through the asymmetric straight flow-through MC, and a continuous water phase fills the microslot and the domain over the slot outlet. The flow of the two phases was considered laminar. Table 1 lists the dimensions of asymmetric straight flow-through MCs with representative sizes expressed as the channel diameter (d_{MC}) of 5 to 400 μm. The control asymmetric straight flow-through MC had a slot of $100 \times 10 \times 30$ μm (x-, y-, and z-directions in Fig. 2) and a channel of $10 \times 10 \times 70$ μm. The domain over the slot was $100 \times 80 \times 70$ μm. This asymmetric straight flow-through MC has dimensions similar to those of the standard asymmetric straight flow-through MCs fabricated in an actual MC emulsification device (WMS1) (Kobayashi et al. 2009). Since the domain depicted in Fig. 2 is symmetrical in the $x = 0$ and $y = 0$ planes, one-fourth of the total domain was modeled as the computational domain (gray domain surrounded by solid lines). *CFD-GEOM* software was used to define the 3D computational domain and to generate the structured grid consisting of 63,474 non-uniform cells (Fig. 3). The cell number was determined based on our previous study that simulated droplet generation via symmetric straight flow-through MCs (Kobayashi et al. 2004). The droplet generation phenomena were appropriately simulated using 3D computational domains with about 40000 cells. As depicted in Fig. 3, the computational domain also has the finest grids in the regions near the channel and slot outlets, since the

velocity of both phases and the pressure would be fastest there.

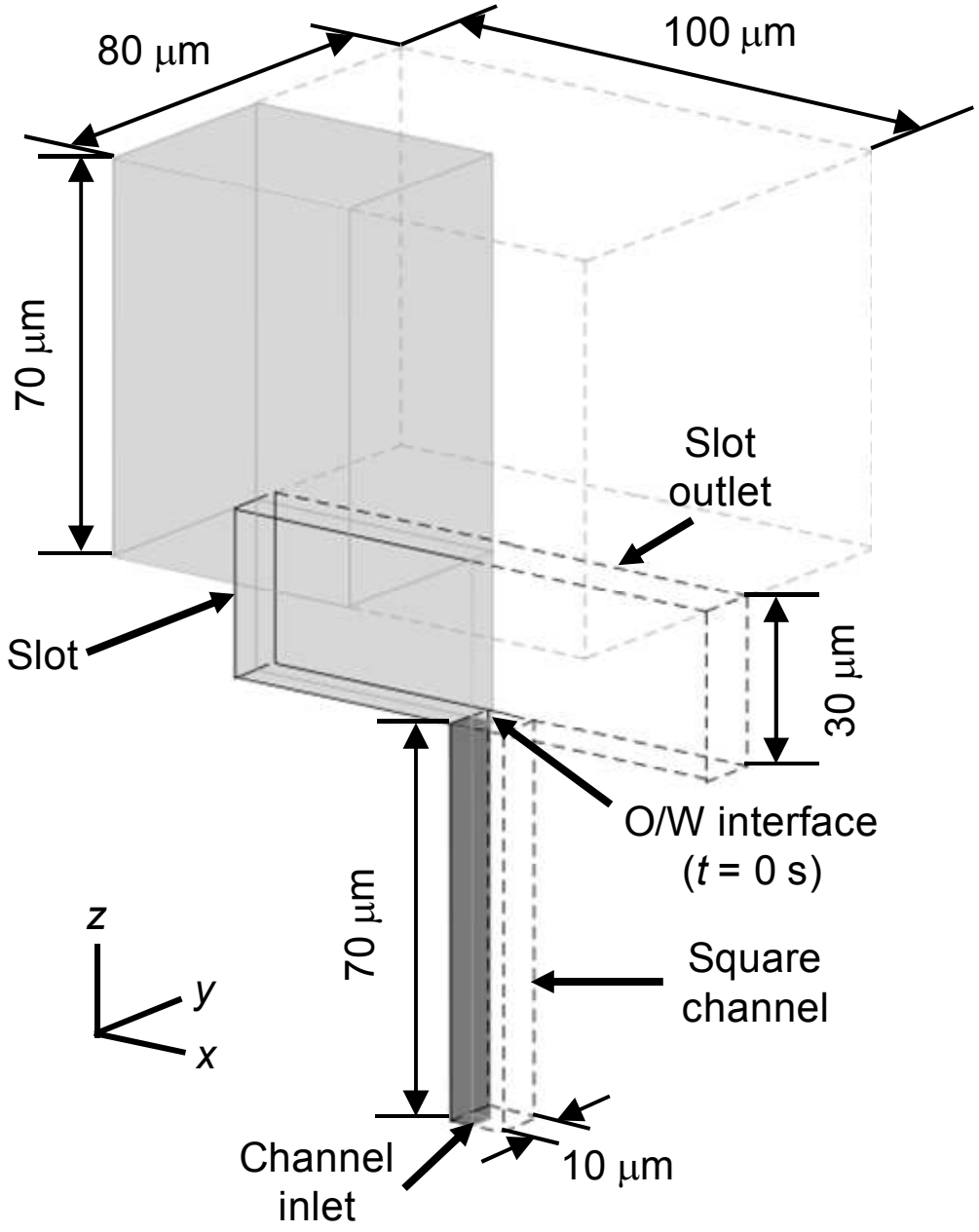

Fig. 2 Three-dimensional drawing of the geometry including a single asymmetric straight flow-through MC, used in the computational problem of this study.

Table 1 Dimensions of asymmetric straight flow-through MCs used in this study.

Channel diameter, d_{MC} [μm]	Channel depth, h_{MC} [μm]	Slot size, $w_{l,slot}$[a] × $w_{s,slot}$[a] [μm]	Slot depth, h_{slot} [μm]
5	35	50 × 5	15
10	70	100 × 10	30
30	210	300 × 30	90
50	350	500 × 50	150
100	700	1 000 × 100	300
150	1 050	1 500 × 150	450
200	1 400	2 000 × 200	600
300	2 100	3 000 × 300	900
400	2 800	4 000 × 400	1 200

[a] $w_{l,slot}$ and $w_{s,slot}$ are the shorter slot width and the longer slot width, respectively.

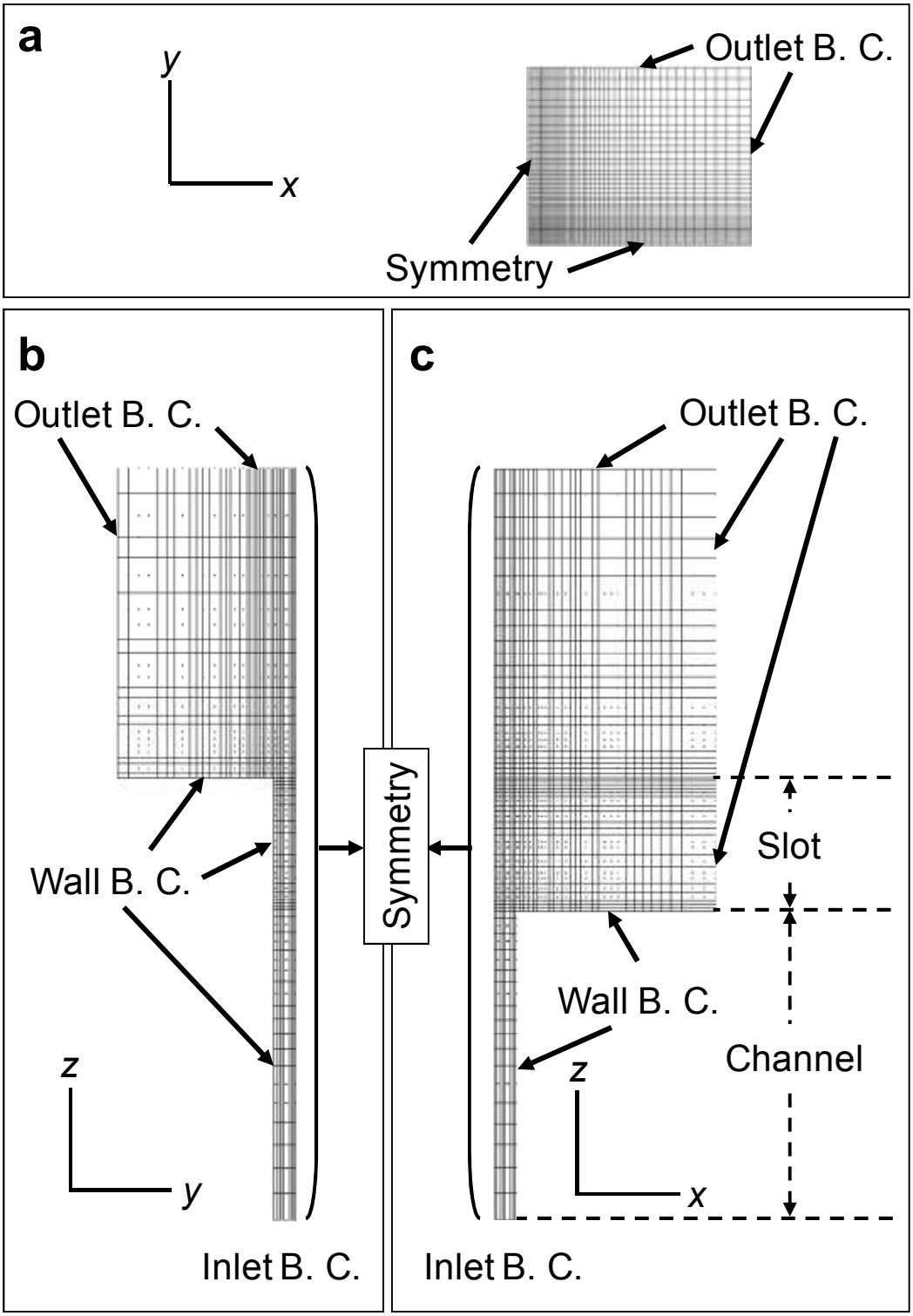

Fig. 3 Structured grid generated in the computational domain and boundary conditions of the computational domain. (a) *x*-*y* plane ($z = 0$). (b) *y*-*z* plane ($x = 0$). (c) *x*-*z* plane ($y = 0$).

2.2. Governing equations

CFD-ACE-GUI software with a finite volume code was used to calculate the governing equations (a continuity equation and a Navier-Stokes momentum conservation equation) for the flow of two incompressible fluids (Kobayashi et al. 2004). The volume of fluid (VOF) method, originally developed by Hirt and Nichols (1981), was used to track the motion of the interface between two fluids. The following passive transport equation enables calculating the volume fraction of fluid *i* (F_i) in each cell:

$$\frac{\partial F_i}{\partial t} + \nabla \cdot UF_i = 0 \tag{1}$$

$$F_1+F_2=1 \tag{2}$$

where U is the fluid velocity and t is time. Piecewise linear interface construction (PLIC) method (Youngs 1982) was applied to reconstruct the interface, which was assumed to be planar and to take any orientation within each cell. For the problem considered here, F_2 takes the value of 1 in cells that contain only a dispersed phase, the value of 0 in cells that contain only a continuous phase, and a value between 0 and 1 in cells that contain an oil-water interface. Interfacial tension forces are incorporated using the method proposed by Yang et al. The net normal force on the interface is assumed to be equal to the summation of interfacial tension forces acting tangentially; therefore, interfacial tension forces can be expressed by the following equation:

$$\int \Delta P d\vec{s} = \int \vec{\tau} \left| d\vec{x} \right| = \int \sigma \vec{n} d\vec{x} \tag{3}$$

where ΔP is the pressure difference between the two phases, $d\vec{s}$ is the area of the interface in a given cell, $\vec{n}$ is the unit vector normal to the interface, and $d\vec{x}$ is the vector representing the intersection of the interface and the face of the cell.

2.3. Fluids

As the control in this study, we chose a two-phase system consisting of refined soybean oil as the dispersed phase and water as the continuous phase. The refined soybean oil had a density of 920 kg m^{-3} and a viscosity of 5.0×10^{-2} Pa s, and the water had a density of 997 kg m^{-3} and a viscosity of 9.1×10^{-4} Pa s. The static interfacial tension (γ) applied in this work was 2.5×10^{-2} N m^{-1} unless otherwise noted. The values of density, viscosity, and interfacial tension were adopted from our previous paper (Kobayashi et al. 2004).

2.4. Computation conditions and procedure

CFD-ACE-GUI software was used to set boundary, initial, and volume conditions and to perform computations. The boundary conditions applied to the computational domain are presented in Fig. 3. A no-slip condition was applied to all the walls in the computational domain, and they were assumed to be fully wetted by the continuous phase with a wall contact angle of 0°(Kobayashi et al. 2004). The outlet planes over the slot were assumed to have a pressure of 100 kPa. An outlet boundary condition was applied to the top and side boundaries in the continuous phase domain. The computational domain with this boundary condition (Fig. 3) indicates that the lateral interactions between adjacent asymmetric straight flow-through MCs are not considered in this study. The initial conditions applied to the computational domain are presented in Fig. 2. At time t = 0 ms, the dispersed phase fills the channel, and the continuous phase fills the slot and the domain over the slot outlet; a flat oil-water interface is positioned at the channel outlet. The dispersed-phase velocity (U_d) at the channel inlet (z-direction) was set in a range of 0.25 to 10.0 mm s^{-1}. No forced crossflow of the continuous phase was applied to the domain over the slot. An initial time step of 1×10^{-3} ms was chosen for the computations. Each time step (except for the initial one) was automatically adjusted after a maximum of 20 iterations. We selected the Courant-Friedrichs-Lewy (CFL) number of 0.2, meaning that the interface can cross a

maximum of 20% of the width of a cell during each time step. The SIMPLEC algorithm (van Doormal 1984) was used as the pressure-velocity coupling scheme. The computations were performed in a single 3.8-GHz Pentium IV processor and 2.0-GB internal memory, taking 2 to 14 days to complete each run.

CFD-VIEW software was used to visualize the numerical output data. The visualized data were used to analyze the droplet generation process via an asymmetric straight flow-through MC and the flow behavior of the two phases during droplet generation. The pressure and velocity distributions during droplet generation were analyzed using the pressure and velocity data extracted from the output data files. The droplet diameter (d_{drop}) was determined by a procedure reported elsewhere (Kobayashi et al. 2004) that calculates d_{drop} based on the droplet volume. The diameter of the first droplet was used as d_{drop}, since this droplet remains the slot outlet in the most cases, which coalesces with the second droplet.

3. Results and discussion

3.1. CFD simulation results for droplet generation process

In this section, we present the CFD simulation results for the droplet generation process via an asymmetric straight flow-through MC, which consists of visualizing the droplet generation process and the effect of interfacial tension during droplet generation. An asymmetric straight flow-through MC with d_{MC} of 10 μm was considered here. Figures 4 and 5 display the CFD simulation results of oil droplet generation via the asymmetric straight flow-through MC at U_d of 1.0 mm s^{-1}. The pressurized dispersed phase gradually expanded inside the slot with a discoid shape until the tip of the dispersed phase reached the slot outlet (Fig. 4a, b). This process was defined as disk expansion. Part of the continuous phase inside the slot was forced to flow outside the slot as the dispersed phase expanded inside the slot

(Fig. 5a, b). The moment depicted in Fig. 4b was defined as the starting point of the detachment process (the detachment time (t_{det}) of 0 ms). The dispersed phase that passed through the slot outlet gradually expanded outside the slot for 35 ms (Fig. 4c). The dispersed phase then dramatically expanded outside the slot, which was associated with the dramatic shrinkage of the dispersed phase inside the slot (Fig. 4c, d). Figure 5d demonstrates that the continuous phase flowed rapidly into the slot, particularly toward the shrinking dispersed phase. Sufficient space for the continuous phase must be maintained at the slot outlet to achieve this behavior, as reported in our previous CFD study on droplet generation via a symmetric straight flow-through MC (Kobayashi et al. 2004). A quasi-circular neck of the dispersed phase was formed inside the slot at t_{det} of 49 ms (Fig. 4e). Eventually, the neck pinched off instantaneously, generating an oil droplet with d_{drop} of 27.5 μm at t_{det} of 52 ms (Fig. 4e, f). After droplet generation, the dispersed phase receded inside the slot, and then began to advance again inside the slot. The CFD simulation results also indicate that the asymmetric straight flow-through MC generate the droplet in the absence of a cross-flowing continuous phase, which is analogous to experimental results using an asymmetric straight flow-through MC array (Kobayashi et al. 2005a).

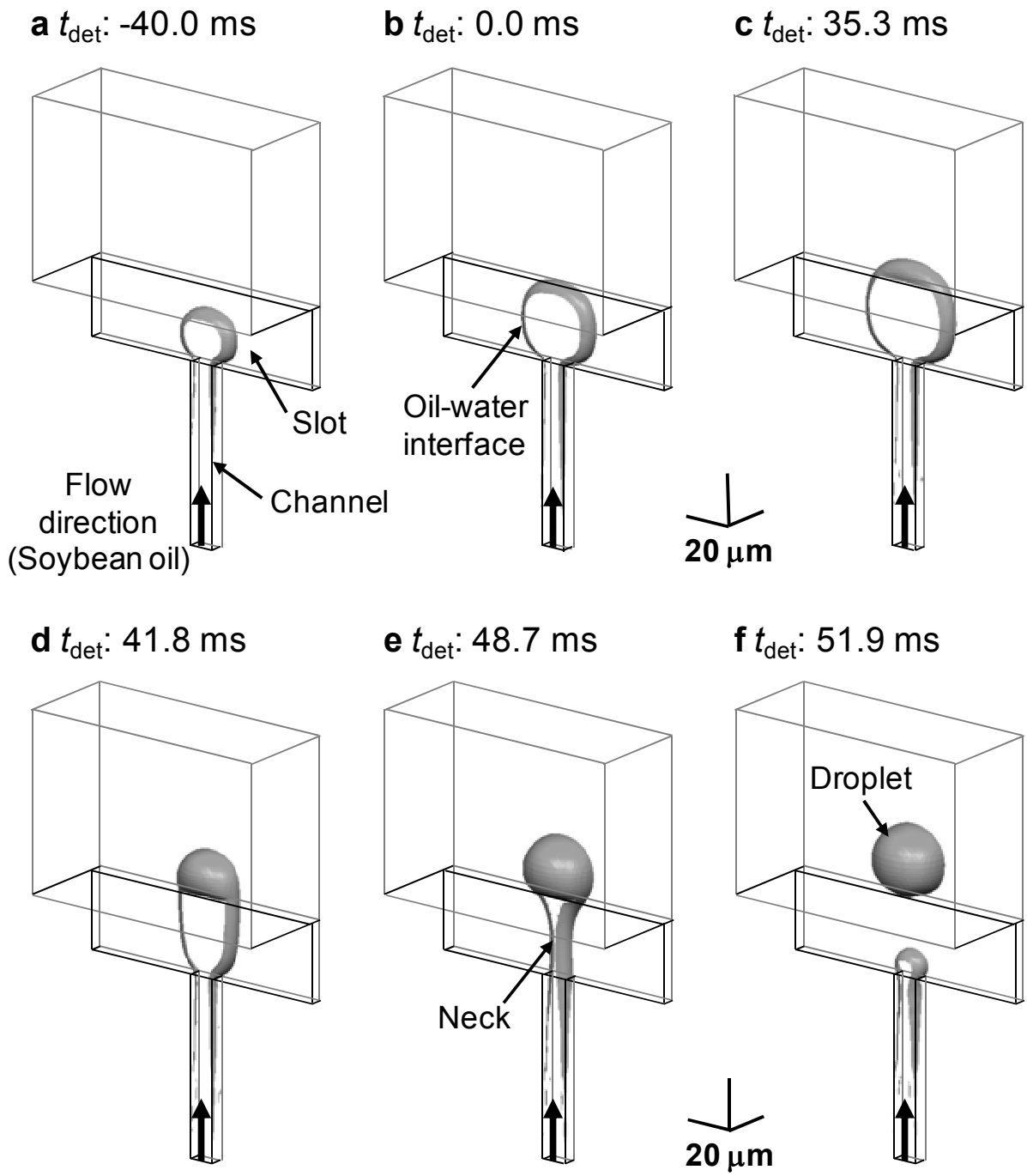

Fig. 4 Typical CFD simulation result of successful droplet generation via an asymmetric straight flow-through MC (t_{det} is the detachment time).

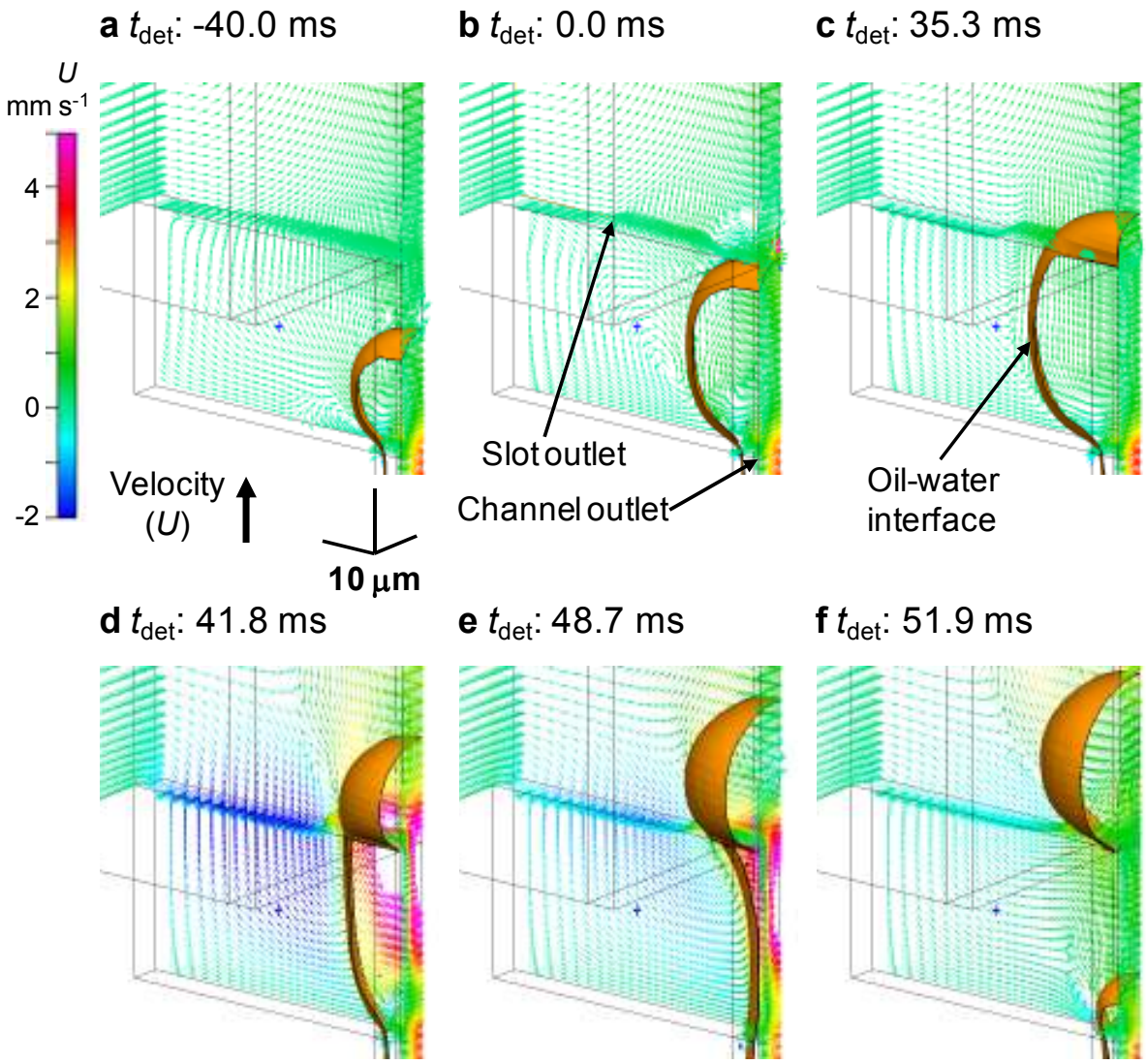

Fig. 5 CFD simulation result for velocity fields during droplet generation via an asymmetric straight flow-through MC. The velocity (U) of the liquids is positive when a liquid flows from bottom to top (t_{det} is the detachment time).

It is difficult to observe the shape of an oil-water interface inside the slot during droplet generation experiments (Kobayashi et al. 2005a). In contrast, emulsification using a grooved MC array enables observing the shape of oil-water interfaces inside the terrace during droplet generation (Sugiura et al. 2001b). A narrow MC and a terrace in a grooved MC array correspond to a channel and a slot in an asymmetric straight flow-through MC. Therefore, the simulated droplet generation process (Fig. 4) can be compared qualitatively with the droplet generation process observed in an experiment using a grooved MC array (Sugiura et al. 2001b). The experiment result reported in the literature demonstrated the gradual expansion of the disk-like dispersed phase inside the terrace, the formation of a neck inside the terrace associated with the rapid shrinkage of the dispersed phase inside the terrace, and the instantaneous pinch-off of the neck that generates an oil droplet. Thus, the visual droplet generation result for the simulation seems to be similar to that for the experiment.

3.2. Effect of interfacial tension

Figure 6 presents the simulation and experimental results for the effect of interfacial tension on the variations of the resultant droplet diameter and the droplet generation frequency. The simulations were conducted at γ of 2.5×10^{-2} N m^{-1} (assuming the absence of a surfactant) and 5.0×10^{-3} N m^{-1} (assuming the presence of a surfactant (e.g., Tween 20) dissolved in the continuous phase at a concentration over the critical micelle concentration). The droplet diameter for simulation at a high γ was independent of U_d, whereas the droplet diameter for simulation at a low γ gradually increased with increasing U_d and dramatically increased at U_d of 1.5 mm s^{-1}. In the range examined, d_{drop} values for simulation at a low γ exceeded those at a high γ. For the simulation, droplet generation frequency at a high γ linearly increased with increasing U_d. In contrast, droplet generation frequency at a low γ slightly increased with increasing U_d in the range of 0.5 to 1.0 mm s^{-1} and decreased with a further increase of U_d in

the range of 1.0 to 1.5 mm s^{-1}. Interestingly, our previous experiment results (Vladisavljević et al. 2006) are in excellent agreement with the simulation results at a high γ (i.e., in the absence of a surfactant). The experiments used a soybean oil-in-a Milli-Q water solution containing Tween 20 (2.0 wt%) system.

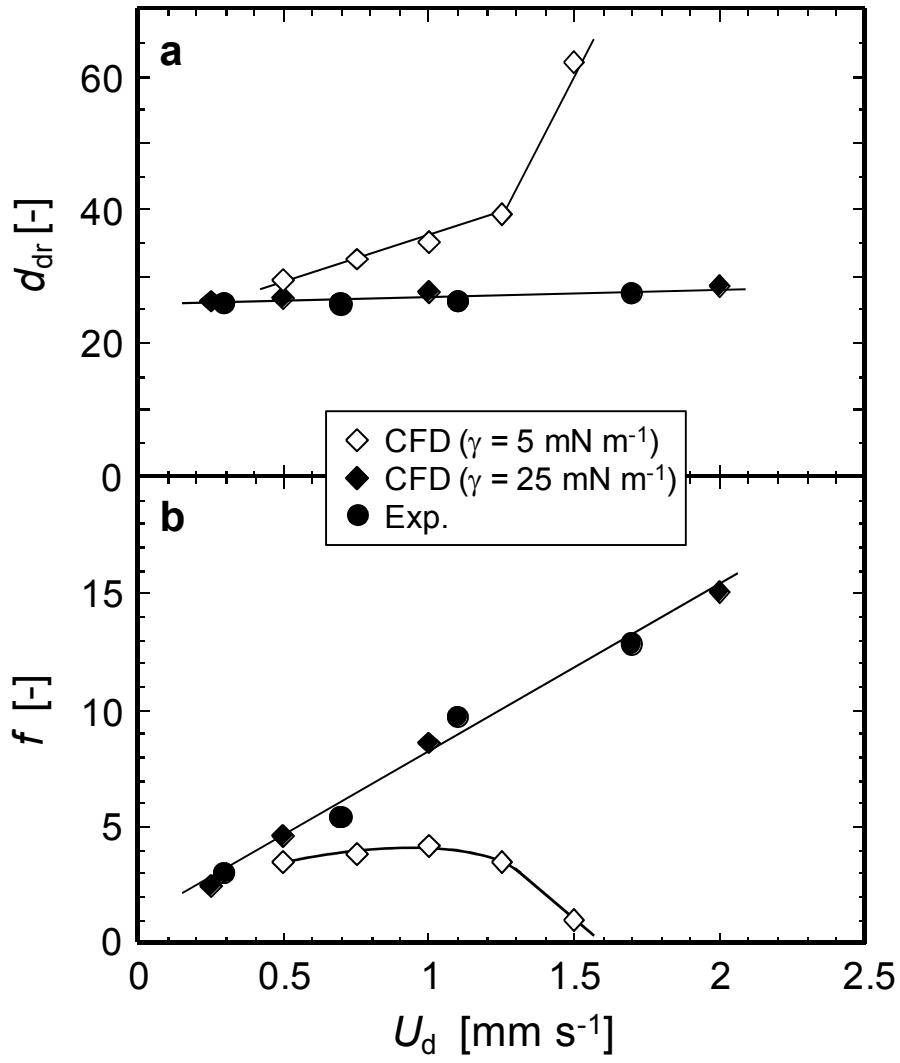

Fig. 6 Variation of droplet diameter (d_{drop}) and droplet generation rate (f) as a function of dispersed-phase velocity (U_d). Here, γ is the interfacial tension between the two phases. The experimental data of Vladisavljević et al. (2006) were used for comparison with the CFD results. Sauter mean diameter ($d_{3,2}$) measured with a light scattering instrument was used as d_{drop} for the experimental results.

This agreement can be explained as follows. When a continuous phase contains surfactant molecules, they adsorb to a freshly generated oil-water interface, dynamically lowering interfacial tension. Dynamic interfacial tension at a vegetable oil-water (2.0 wt% Tween 20) interface was measured by Schröder et al. (1998) using the bursting membrane method. Dynamic interfacial tension sharply decreased within 2 s, ultimately reaching an almost constant value. Their measurement data also indicated that dynamic interfacial tension hardly changed on a time scale of less than 100 ms, which corresponds to the detachment time for the simulation and experiment results compared in this work. This indicates that the interfacial tension during detachment process is close to the interfacial tension at the pure oil-water interface. In addition, the Tween 20 concentration (0 and 1.0 wt%) in the continuous phase did not affect the size of the soybean oil droplets generated by MC emulsification experiments (Kobayashi et al. 2002b). In contrast, a previous MC emulsification study demonstrated that the size of oil droplets increased as the interfacial tension decreases when using viscous oils and a rapidly adsorbing surfactant (sodium dodecyl sulfate) (Kobayashi et al. 2005b). It was therefore confirmed that the decrease in dynamic interfacial tension would be negligible during droplet generation via asymmetric straight flow-through MCs reported here, due to the short detachment time.

3.3. CFD analysis of the detachment process

In this section, we used the data obtained from the CFD simulations to analyze the detachment process, which includes the most important phenomena during droplet generation by MC emulsification. Figure 7 presents the variation of internal pressures of the dispersed phase as a function of time obtained from the CFD simulations. The positions of the dispersed phase considered here were the centers of the channel outlet, the dispersed phase in the slot, and the dispersed phase over the slot. In Fig. 7a, the internal pressures of the dispersed phase

in and over the slot can be approximated by the Laplace pressures acting on an oil-water interface in and over the slot.

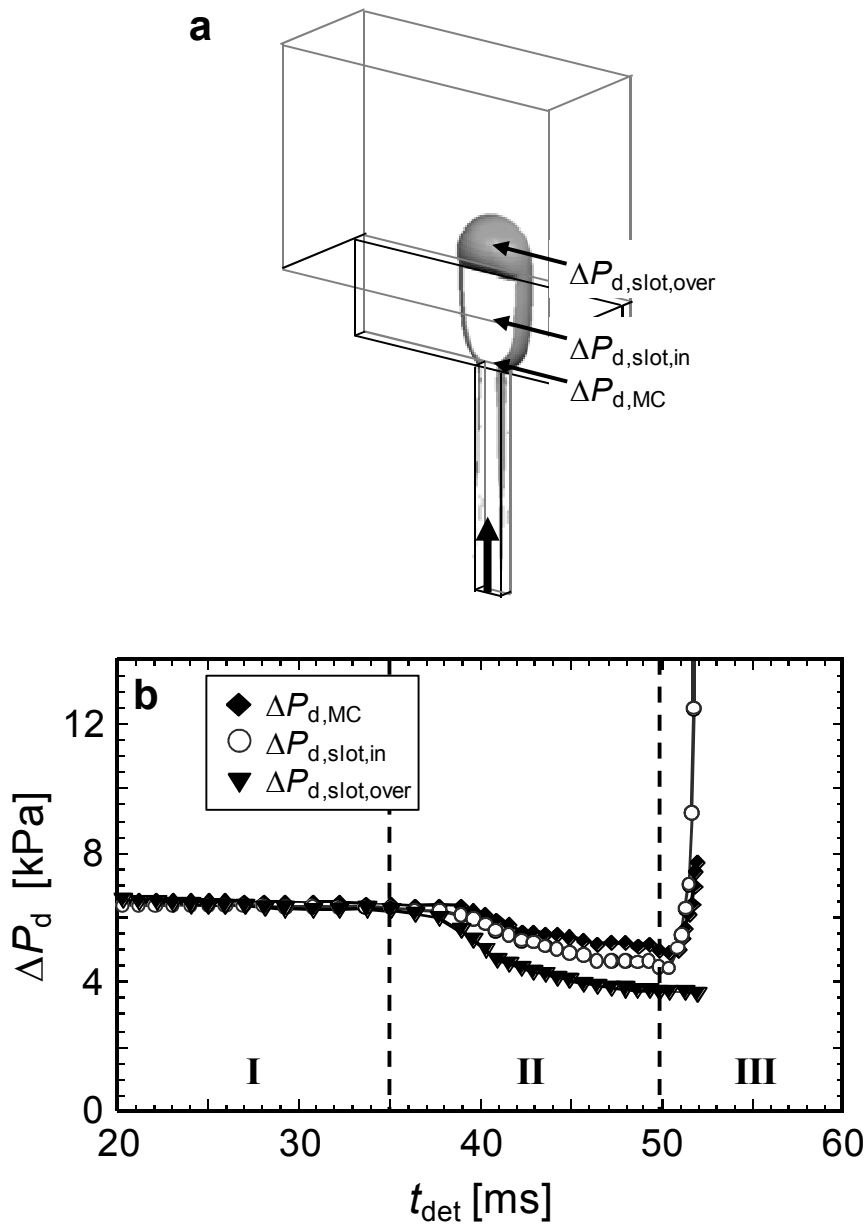

Fig. 7 (a) Three-dimensional snapshot of the oil-water interface during the detachment process obtained from a CFD simulation data. Here, $\Delta P_{d,MC}$ is the internal pressure of the dispersed phase at the channel outlet, $\Delta P_{d,slot,in}$ is the internal pressure of the dispersed phase

in the slot, and $\Delta P_{d,slot,over}$ is the internal pressure over the slot. (b) Variation of $\Delta P_{d,MC}$, $\Delta P_{d,slot,in}$, and $\Delta P_{d,slot,over}$ as a function of detachment time (t_{det}).

In stage I of the detachment process (t_{det} = <35 ms), the internal pressures of the dispersed phase at the channel outlet ($\Delta P_{d,MC}$) and in the slot ($\Delta P_{d,slot,in}$) hardly changed, whereas the internal pressure of the dispersed phase over the slot ($\Delta P_{d,slot,over}$) decreased slowly with time. This stage is considered to be driven by the inflow of the dispersed phase from the channel outlet. These trends in the internal pressures of the dispersed phase reasonably reflect the change of the oil-water interface in and over the slot (Fig. 4b, c). Although $\Delta P_{d,slot,over}$ was higher than $\Delta P_{d,slot,in}$ at t_{det} of 20 ms, $\Delta P_{d,slot,over}$ became lower than $\Delta P_{d,slot,in}$ at t_{det} of 35 ms, triggering stage II of the detachment process.

In stage II (t_{det} = 35 to 50 ms), all the internal pressures of the dispersed phase gradually decreased with time. Here, $\Delta P_{d,MC}$ decreased by 22.1%, $\Delta P_{d,slot,in}$, decreased by 29.0%, and $\Delta P_{d,slot,over}$ decreased by 40.3%. In this case, the balance among the internal pressures of the dispersed phase can be expressed as

$$\Delta P_{d,MC} > \Delta P_{d,slot,in} > \Delta P_{d,slot,over} \quad (4).$$

The imbalance between $\Delta P_{d,slot,in}$ and $\Delta P_{d,slot,over}$ in this equation causes rapid expansion of the dispersed phase over the slot and rapid shrinkage of the dispersed phase in the slot, which confirms the experiment results reported by Sugiura et al. (2001b). This process may not be influenced by the inflow of the dispersed phase from the channel outlet. When a quasi-circular neck forms in the slot at t_{det} of 50 ms (Fig. 4e), the flux balance of the dispersed phase near the neck becomes an important factor (van Dijke et al. 2008). The outflow of the dispersed phase from the quasi-circular neck increases gradually with time, since $\Delta P_{d,slot,over}$ continues to decrease as the size of the expanding dispersed phase increases. In contrast, the inflow of the dispersed phase from the channel outlet to the quasi-circular neck does not increase due to the almost unchanged difference between $\Delta P_{d,MC}$ and $\Delta P_{d,slot,in}$. At the moment when the flux of the preceding outflow becomes dominant, the pinch-off of the neck (stage III) is triggered. Thus, the transition from stage II to stage III is supposed to be dominated by the flow of the

dispersed phase near the quasi-circular neck.

In stage III (t_{det} = >50 ms), $\Delta P_{d,MC}$ and $\Delta P_{d,slot,in}$ increased steeply, whereas $\Delta P_{d,slot,over}$ decreased slightly. In this case, the balance among the internal pressures of the dispersed phase changed as follows:

$$\Delta P_{d,slot,in} > \Delta P_{d,MC} > \Delta P_{d,slot,over} \quad (5).$$

The difference between $\Delta P_{d,slot,in}$ and $\Delta P_{d,slot,over}$ is large enough to cause the immediate pinch-off of the neck. The dispersed phase ahead of the neck flowed rapidly toward the slot outlet. By contrast, the dispersed phase behind the neck flowed rapidly toward the channel outlet, which was the opposite of its initial flow direction. The preceding results indicate that this stage is not influenced by the inflow of the dispersed phase from the channel outlet. As a result, the oil-water interface in the slot split, leading to the generation of a droplet (Fig. 4f).

CFD analysis conducted in this section demonstrates that the detachment process during droplet generation by MC emulsification can be divided into three important stages. The internal pressure and/or flux balances of the dispersed phase in and over the slot are key factors triggering the transition between two consecutive stages.

3.4. Effect of channel size

3.3.1. Droplet size

Figure 8 depicts the CFD simulation results for the effects of U_d and the size of asymmetric straight flow-through MCs on the dimensionless droplet diameter ($\bar{d}_{drop}$) defined as d_{drop}/d_{MC}. Capillary number of the dispersed phase (Ca_d) was also used as the horizontal axis, since Ca_d is assumed to be the appropriate determining factor for the flow state during droplet generation by MC emulsification (Sugiura et al. 2002b). Here, $\bar{d}_{drop}$ and its variation were independent of d_{MC} in the range of 100 μm or less (Fig. 8a), and $\bar{d}_{drop}$ at a low U_d of 1.0 mm s^{-1} was 2.8, slightly increasing with the increase of U_d below a critical value of 6.0 mm s^{-1}.

At the critical U_d, Ca_d was 0.012. In contrast, in a range of U_d exceeding the critical value, a steep increase in $\bar{d}_{drop}$ is observed and $\bar{d}_{drop}$ is sensitive to U_d, indicating that it becomes difficult to generate uniform droplets. The trends in $\bar{d}_{drop}$ were similar to the MC emulsification results using MC arrays with different channel diameters (Sugiura et al. 2002b). Critical U_d was also found for channels with d_{MC} of 150 and 200 μm (Fig. 8b), whereas its values were somewhat higher than the critical U_d for smaller channels (Fig. 8a). The variation of $\bar{d}_{drop}$ above the critical U_d decreased with increasing d_{MC} above 100 μm. Below the critical U_d, $\bar{d}_{drop}$ and its variation for channels with d_{MC} of 200 μm or less were analogous to those for the smaller channels depicted in Fig. 8a. When channels with d_{MC} of 300 μm or more were used, no steep change in U_d was observed in the range examined, suggesting that no critical U_d exist. The simulation results in Fig. 8 demonstrate that $\bar{d}_{drop}$ and its variation are independent of the size of asymmetric straight flow-through MCs below the critical U_d, which is not the case for large channels with d_{MC} of 300 μm or more.

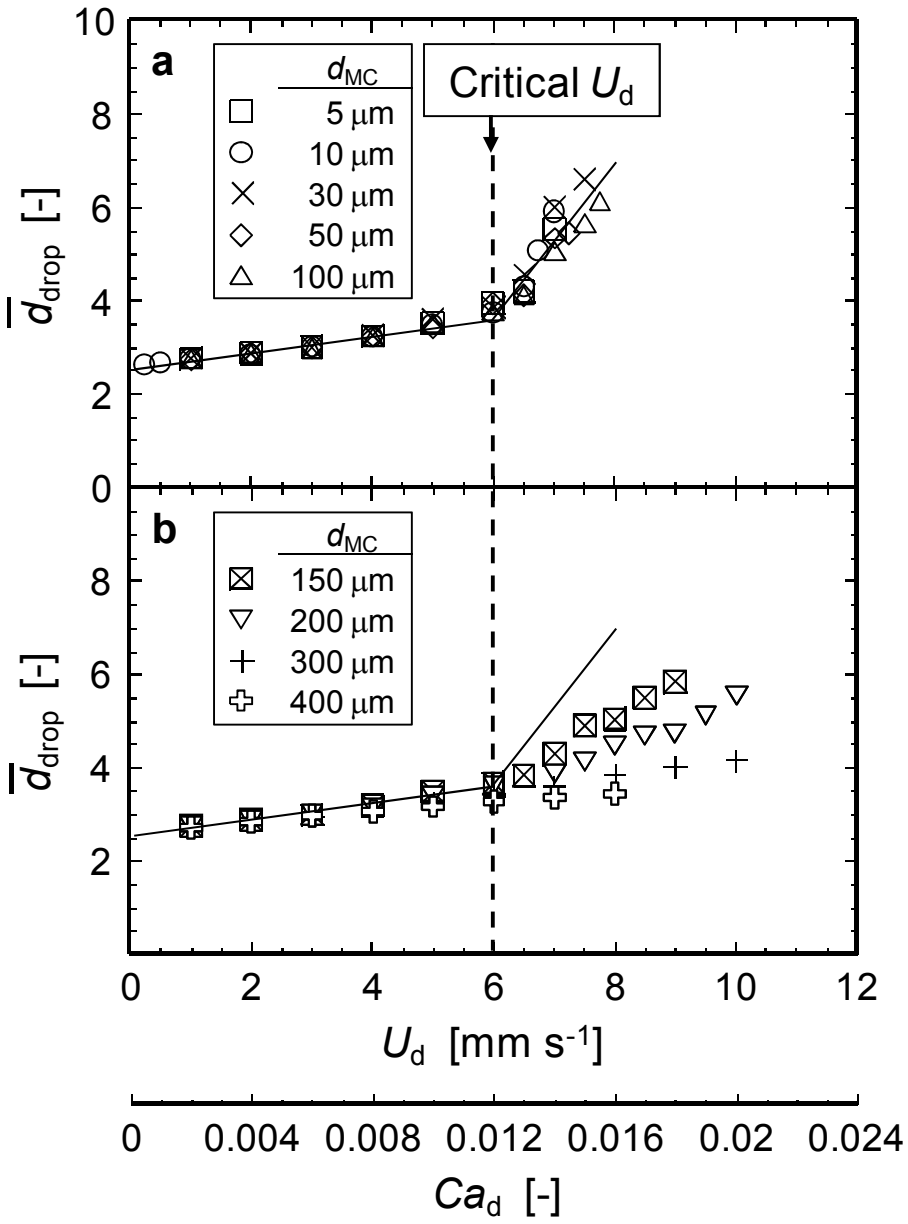

Fig. 8 Variation of dimensionless droplet diameter ($\bar{d}_{drop}$) obtained from the CFD simulations as a function of dispersed-phase velocity (U_d); effect of channel size. Here d_{MC} is the channel diameter and Ca_d is the Capillary number of the dispersed phase that flows in a channel.

Here, the CFD simulation results in Fig. 8 are discussed based on a dimensionless number and the forces acting on a dispersed-phase droplet that expands over a slot. The existence of the critical U_d near which the trend in $\bar{d}_{drop}$ dramatically changes is related to the balance between viscous force and interfacial tension (i.e., Ca_d) (Sugiura et al. 2002b). Below the critical Ca_d, droplet generation is driven by interfacial tension. Above the critical Ca_d, both viscous force and interfacial tension affect droplet generation, leading to the generation of larger droplets. The critical Ca_d values in Fig. 8 were the same order of magnitude as those obtained from MC emulsification experiments (Vladisavljević et al. 2006), validating the simulation results obtained in this study. The variations of $\bar{d}_{drop}$ above the critical U_d can be explained by the balance of buoyancy force (F_B), viscous force (F_V), inertial force (F_I), and interfacial tension force (F_γ), which acts on an expanding dispersed-phase droplet (Fig. 9a). These forces are expressed by the following equations:

$$F_B = \frac{\pi}{6} d_{drop}^3 g \Delta\rho \propto d_{MC}^3 \quad (6)$$

$$F_V = \mu_d d_{MC} U_d \quad (7)$$

$$F_I = \frac{\pi}{3} \rho_d d_{MC}^2 U_d^2 \quad (8)$$

$$F_\gamma = \pi d_{neck} \gamma \cong \pi d_{MC} \gamma \quad (9)$$

where g is the acceleration due to gravity, $\Delta\rho$ is the density difference between the two phases, μ_d is the dispersed-phase viscosity, ρ_d is dispersed-phase density, and d_{neck} is the diameter of a neck formed in the slot. Droplet generation is promoted by F_B, F_V, and F_I but is restricted by F_γ at the neck. The values of F_B, F_V, F_I and F_γ estimated using the preceding equations are plotted in Fig. 9b. Here, F_γ was greater than F_B , F_V, and F_I regardless of channel size. At U_d of 1 mm s^{-1}, the ratio of the promotion forces ($F_B + F_V + F_I$) to the restriction force (F_γ) had a maximum value of 1.8×10^{-2} (Fig. 9c), indicating that the effect of the promotion forces is negligible. At U_d of 7 mm s^{-1}, the preceding force ratio becomes much greater than 10^{-2} for

channels with d_{MC} larger than 100 μm (Fig. 9c), and the effect of the promotion forces must be considered for droplet generation via large channels. We assume that the promotion forces contribute to the lower variation of $\bar{d}_{drop}$ for large channels at U_d above the critical value.

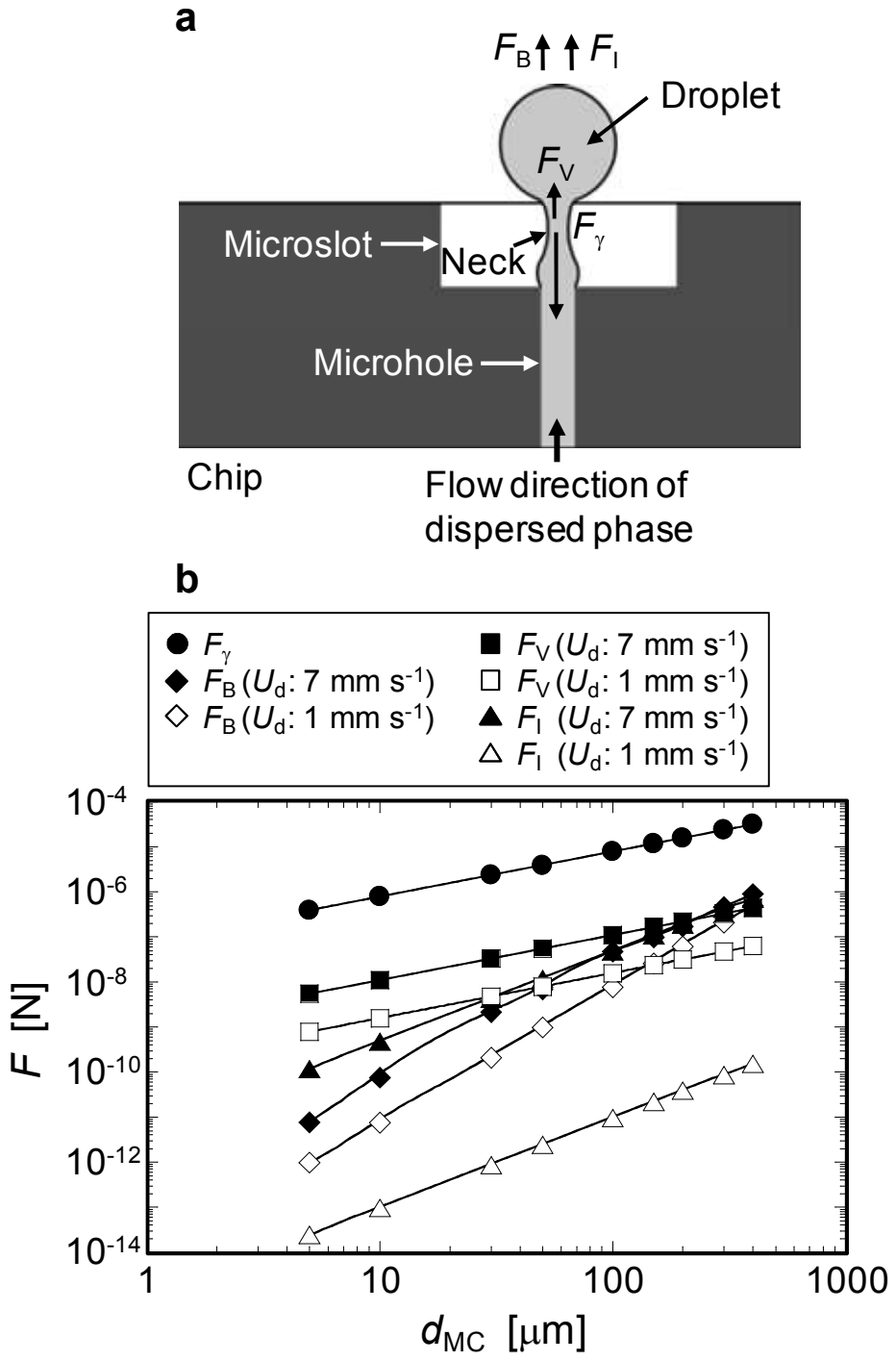

Fig. 9

KOBAYASHI *et al.*

Fig. 9 (a) Schematic drawing of the main forces acting on a dispersed-phase droplet that expands over the slot outlet. Here, F_B is the buoyancy force, F_V is the viscous force, F_I is the

inertial force exerted by a dispersed phase flowing out from an MC, and F_γ is the interfacial tension force. (b) Variation of F_B, F_V, F_I, and F_γ with channel diameter (d_{MC}).

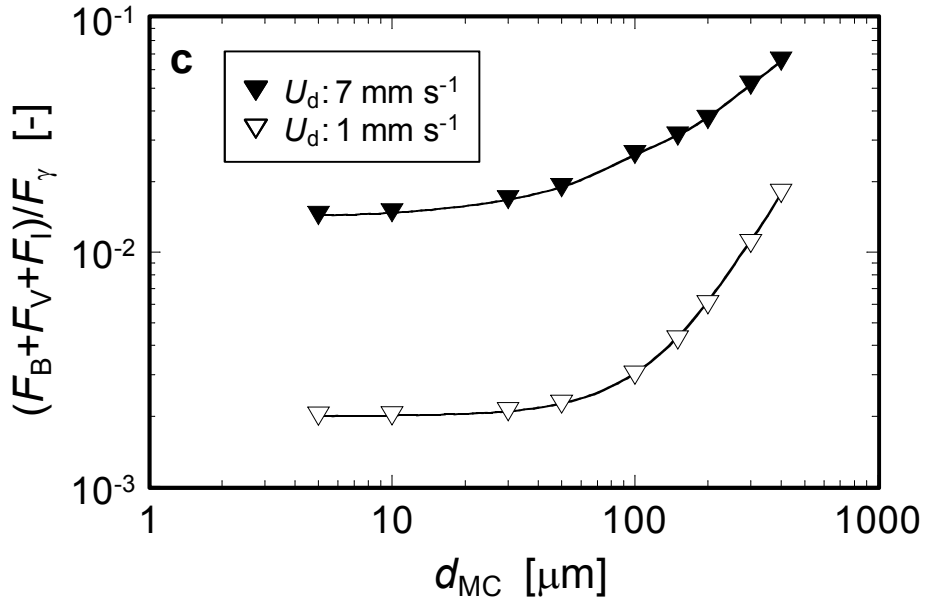

Fig. 9 (c) Variation of the force ratio (($F_B + F_V + F_I$) / F_γ) with d_{MC}.

3.3.2. Droplet production rate

Figure 10a illustrates the CFD simulation results for the effect of U_d and channel size on droplet generation rate (f). For channels with d_{MC} of 200 μm or less, f increased with increasing U_d below the critical value, and f values at a given U_d were inversely proportional to channel size. Conversely, f decreased with increasing U_d in the range above the critical value, which was remarkable for channels with d_{MC} of 100 μm or less. Maximum f values were obtained at U_d near the critical value. For channels with d_{MC} of 300 μm or more, f slowly increased with increasing at low U_d values and hardly changed at high U_d. The data of the maximum droplet generation rate (f_{max}) obtained from the simulations are plotted in Fig. 10b. Here, f_{max} for channels with d_{MC} below 100 μm was inversely proportional to d_{MC} as expressed by the following equation:

$$f_{max} = 2.1 \times 10^2 \, d_{MC}^{-1} \quad (10).$$

However, f_{max} for channels with d_{MC} over 100 μm was higher than that predicted by eq. 10, especially for large channels with d_{MC} of 300 μm or more, because f_{max} for these channels was obtained at U_d higher than that when using channels with d_{MC} below 100 μm. As a result, d_{MC} was found to be a parameter that greatly affects f_{max}.

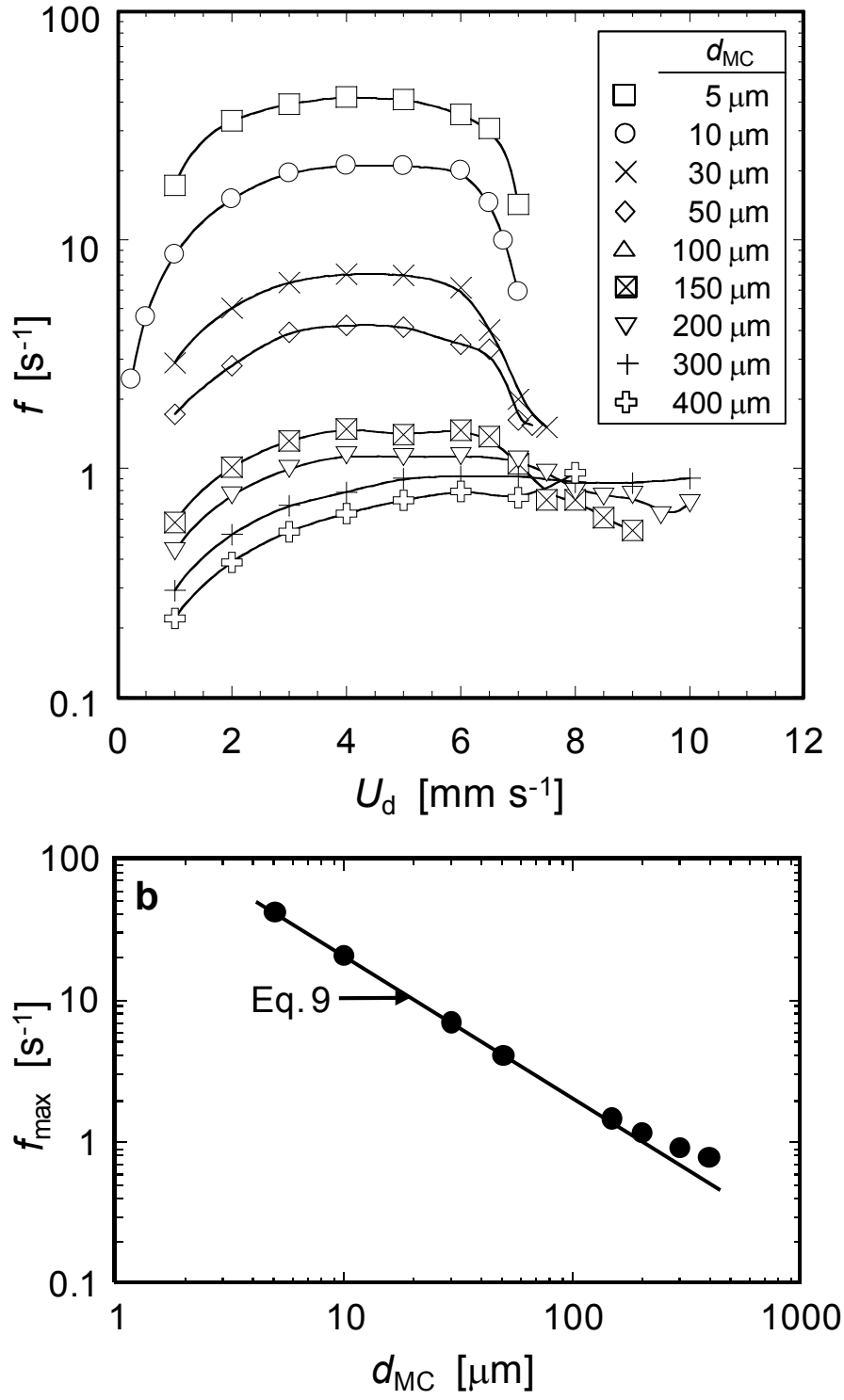

Fig. 10

KOBAYASHI *et al.*

Fig. 10 (a) Variation of the droplet generation rate (f) obtained from the CFD simulations with dispersed-phase velocity (U_d). (b) Variation of the maximum droplet generation rate (f_{max}) with d_{MC}.

The maximum volume flow rate of the droplets generated from each channel (Q_{MC}) is calculated using the following equation:

$$Q_{max,MC} = \frac{\pi}{6} d_{drop}^3 f_{max} \propto d_{MC}^3 \cdot \frac{1}{d_{MC}} = d_{MC}^2 \quad (10).$$

Parameter f_{max} is inversely (or almost inversely) proportional to channel size (Fig. 9b), and $\bar{d}_{drop}$ is independent of channel size (Fig. 8). Therefore, the maximum volume flow rate of the droplets generated from each channel becomes quadratically proportional to the channel size as expressed by eq. 10. The maximum volume flow rate of the droplets produced from an MC array ($Q_{max,MCA}$), is defined as

$$Q_{max,MCA} = N_{MC} Q_{max,MC} \quad (11)$$

where N_{MC} is the number of channels. $Q_{max,MCA}$ per a unit area of MC array is given by

$$\frac{Q_{max,MCA}}{A_{MCA}} = \frac{N_{MC} Q_{max,MC}}{A_{MCA}} \propto \frac{1}{d_{MC}^2} \cdot d_{MC}^2 = \text{constant} \quad (12)$$

where A_{MCA} is the area of an MC array. Asymmetric straight flow-through MCs are compactly arranged as many as possible (Fig. 1a), and the number of channels per unit area is usually designed to quadrically decrease with increasing the channel size (Kobayashi et al. 2010). Considering this relationship, Eq. 12 suggests that the maximum droplet productivity per a unit area (i.e., the maximum dispersed-phase flux) is basically independent of channel size. In contrast, $Q_{max,MCA}$ depends on the total area of MC array(s) fabricated on an MC emulsification device. It is noteworthy that the maximum percentage of active channels generating uniform droplets greatly decreased for channels with d_{MC} smaller than 10 μm, resulting in lower droplet productivity (Kobayashi et al. 2002a; 2005c).

4. Summary

The 3D CFD simulations performed in this study can reasonably well model the whole droplet generation process via an asymmetric straight flow-through MC, which does not require a forced continuous-phase flow. The shape and movement of an oil-water interface during droplet generation were appropriately simulated using CFD. The flow profile of the two phases and the internal pressure balance of the dispersed phase during droplet generation reported in this study provide useful insight into the key phenomena necessary for successful droplet generation via an asymmetric straight flow-through MC. In particular, we found that the detachment process can be divided into three important stages. The comparison between CFD and experimental results for the effect of interfacial tension indicated that dynamic interfacial tension did not decrease during droplet generation because the detachment time was too short to allow surfactant adsorption onto a freshly generated oil-water interface.

The droplet size obtained at a low $U_{d,MC}$ was proportional to the size of the asymmetric straight flow-through MCs used in this study. The critical $U_{d,MC}$, where the trend in variation of $\bar{d}_{drop}$ greatly changes, was observed for channels with d_{MC} of 200 μm or less, whereas no great change in the slope of $\bar{d}_{drop}$ vs. $U_{d,MC}$ line was observed for channels with d_{MC} of 300 μm or more. The difference in these trends in $\bar{d}_{drop}$ can be explained by the force balance of a dispersed-phase droplet that expands over a slot, especially the considerable size dependency of F_B that promotes droplet generation. The maximum droplet generation rate per channel was in principle inversely proportional to the characteristic channel size but was somewhat influenced by the force balance during droplet generation. The maximum droplet volume productivity per unit area of an asymmetric straight flow-through MC array was estimated to be independent of the characteristic channel size. The findings obtained here are expected to be useful for appropriately performing droplet generation via asymmetric straight

flow-through MCs and designing future asymmetric straight flow-through MC arrays.

Acknowledgments

This work was supported in part by the Food Nanotechnology Project of the Ministry of Agriculture, Forestry and Fisheries of Japan.

References

Abate, A.R., Poitzsch, A., Hwang, Y., Lee, J., Czerwinska, J., Weitz, D.A., 2009. Impact of inlet channel geometry on microfluidic drop formation. Phys. Rev. E 80, 026310.

Anna, S.L., Bontoux, N., Stone, H.A., 2003. Formation of dispersions using "flow focusing" in microchannels. Appl. Phys. Lett. 82, 364–366.

de Menech, M., Garstecki, P., Jousse, F., Stone, H.A., 2008. Transition from squeezing to dripping in a microfluidic T-shaped junction. J. Fluid. Mech., 595, 141–161.

Hirt, C.W., Nichols, B.D., 1981. Volume of Fluid (VOF) method for dynamics of free boundaries. J. Comput. Phys. 39, 201–225.

Garstecki, P., Fuerstman, M.J., Stone, H.A., Whitesides, G.M., 2006. Formation of droplets and bubbles in a microfluidic T-junction–scaling and mechanism of break-up. Lab Chip 6, 437–446.

Günther, A., Jensen, K.F., 2006. Multiphase microfluidics: from flow characteristics to chemical and materials synthesis. Lab Chip 6, 1483–1503.

Gupta, A., Kumar, R., 2010. Effect of geometry on droplet formation in the sqeezing regime in a microfluidic T-junction. Microfluid. Nanofluid. 8, 799–812.

Kashid, M.N., Renken, A., Kiwi-Minsker, L., 2010. CFD modeling of liquid-liquid multiphase microstructured reactor: slug flow generation. Chem. Eng. Res. Des., 88, 362–368.

Kawakatsu, T., Kikuchi, Y., Nakajima, M., 1997. Regular-sized cell creation in microchannel emulsification by visual micro-processing method. J. Am. Oil Chem. Soc. 74, 317–321.

Kawakatsu, T., Komori, H., Nakajima, M., Kikuchi, Y., Yonemoto, T., 1999. Production of monodispersed oil-in-water emulsion using crossflow-type silicon microchannel plate. J. Chem. Eng. Japan 32, 241–244.

Kobayashi, I., Nakajima, M., Chun. K., Kikuchi. Y., Fujita, F., 2002a. Silicon array of

elongated through-holes for monodisperse emulsions. AIChE J. 48, 1639–1644.

Kobayashi, I., Nakajima, M., 2002b. Effect of emulsifiers on the preparation of food-grade oil-in-water emulsions using a straight-through extrusion filter. Eur. J. Lipid Sci. Technol. 104, 720–727.

Kobayashi, I., Nakajima, M., Mukataka, S., 2003. Preparation characteristics of oil-in-water emulsions using differently charged surfactants in straight-through microchannel emulsification. Colloids Surf. A: Physicochem. Eng. Aspects 229, 33–41.

Kobayashi, I., Mukataka, S., Nakajima, M., 2004. CFD simulation and analysis of emulsion droplet formation from straight-through microchannels. Langmuir 20, 9868–9877.

Kobayashi, I., Mukataka, S., Nakajima, M. 2005a. Novel asymmetric through-hole array microfabricated on a silicon plate for formulating monodisperse emulsions. Langmuir 21, 7629–7632.

Kobayashi, I., Mukataka, S., Nakajima, M., 2005b. Effects of type and physical properties of oil phase on oil-in-water emulsion droplet formation in straight-through microchannel emulsification: Experimental and CFD studies. Langmuir 21, 5722-5730.

Kobayashi, I., Mukataka, S., Nakajima, M., 2005c. Production of monodisperse oil-in-water emulsions using a large silicon straight-through microchannel plate. Ind. Eng. Chem. Res. 44, 5852–5856.

Kobayashi, I., Uemura, K., Nakajima, M., 2006. CFD study of the effect of fluid flow in a channel on generation of oil-in-water emulsion droplets in straight-through microchannel emulsification. J. Chem. Eng. Japan 39, 855–863.

Kobayashi, I., Uemura, K., Nakajima, M., 2007. Formulation of monodisperse emulsions using submicron-channel arrays. Colloids Surf. A: Physicochem. Eng. Aspects 296, 285–289.

Kobayashi, I., Murayama, Y., Kuroiwa, T., Uemura, K., Nakajima, M., 2009. Production of

monodisperse water-in-oil emulsions consisting of highly uniform droplets using asymmetric straight-through microchannel arrays. Microfluid. Nanofluid. 7, 107–119.

Kobayashi, I., Hori, Y., Uemura, K., Nakajima, M., 2010. Production characteristics of large soybean oil droplets by microchannel emulsification using asymmetric through holes. Japan J. Food Eng. 11, 34–48.

Li, W., Greener, J., Voicu, D., Kumacheva, E., 2009. Multiple modular microfluidic (M^3) reactors for the synthesis of polymer particles. Lab Chip 9, 2715–2721.

McClements, D.J., 2004. Food Emulsions: Principles, Practice and Techniques. 2nd ed. CRC Press, Boca Raton, chapter 6

Nakagawa, K., Iwamoto, S., Nakajima, M., Shono, A., Satoh, K., 2004. Microchannel emulsification using gelatin and surfactant-free coacervate microencapsulation. J. Colloid Interface Sci. 278, 198–205.

Nie, Z., Li, W., Seo, M., Xu, S., Kumacheva, E., 2006. Janus and ternary perticles generated by microfluidic synthesis: design, synthesis, and self-assembly. J. Am. Chem. Soc. 128, 9408–9412.

Nishisako, T., Torii, T., Higuchi, T., 2002. Droplet formation in a microchannel network. Lab Chip 2, 24–26.

Nishisako, T., Torii. T., 2007. Formation of biphasic janus droplets in a microfabricated channel for the synthesis of shape-controlled polymer microparticles. Adv. Mater. 19, 1489–1493.

Nishisako, T., Torii, T., 2008. Microfluidic large-scale integration on a chip for mass production of monodisperse droplets and particles. Lab Chip 8, 287–293.

Rayner, M., Trägårdh, G., Trägårdh, C., Dejmek, P., 2004. Using the surface evolver to model droplet formation processes in membrane emulsification. J. Colloid Interface Sci. 279, 175–185.

Sang, L., Hong, Y., Wang, F., 2008. Investigation of viscosity effect on droplet formation in T-shaped microchannels by numerical and analytical methods. Microfluid. Nanofluid. 6, 621–635.

Schröder, V., Behrend, O., Schubert, H., 1998. Effect of dynamic interfacial tension on the emulsification process using microporous ceramic membranes. J. Colloid Interface Sci. 202, 334–340.

Seiffert, S., Thiele, J., Abate, A.R., Weitz, D.A., 2010. Smart microgel capsules from macromolecular precursors. J. Am. Chem. Soc. 132, 6606–6609.

Sugiura, S., Nakajima, M., Itoh, H., Seki, M., 2001a. Synthesis of polymeric microspheres with narrow size distributions employing microchannel emulsification. Macromol. Rapid Commun. 227, 773–778.

Sugiura, S., Nakajima, M., Iwamoto, S., Seki, M., 2001b. Interfacial tension driven monodispersed droplet formation from microfabricated channel array. Langmuir 17, 5562–5566.

Sugiura, S., Nakajima, M., Seki, M., 2002a. Prediction of droplet diameter for microchannel emulsification. Langmuir 18, 3854–3859.

Sugiura, S., Kumazawa, N., Nakajima, M., Seki, M., 2002b. Characterization of spontaneous transformation-based droplet formation during microchannel emulsificaiton. J. Phys. Chem. B 17, 5562–5566.

Sugiura, S., Kuroiwa, T., Kagora, T., Nakajima, M., Sato, S., Mukataka, S., Walde, P., Ichikawa, S., 2008. Novel method for obtaining homogeneous giant vesicles from a monodisperse water-in-oil emulsion prepared with a microfluidic device. Langmuir 24, 4581–4588.

Tetradis-Meris, G., Rossetti, D., de Torres, C.P., Cao, R., Lian, G., Janes, R., 2009. Novel parallel integration of microfluidic device network for emulsion formation. Ind. Eng.

Chem. Res. 48, 8881–8889.

Thorsen, T., Roberts, E.W., Arnold, F.H., Quake, S.R., 2001. Dynamic pattern formation in a vesicle-generating microfluidic device. Phys. Rev. Lett. 86, 4163–4166.

Utada, A.S., Lorenceau, E., Link, D.R., Kaplan, P.D., Stone, H.A., Weitz, D.A., 2005. Monodisperse double emulsions generated from a microfluidic device. Science 308, 537–541.

van der Zwan, E., van der Sman, R., Schören, K., Boom, R., 2009. Lattice Boltzmann simulations of droplet during microchannel emulsification. J. Colloid Interface Sci. 335, 112–122.

van Dijke, K.C., Schören, K.C.P.G.H., Boom, R.M., 2008. Microchannel emulsification: from computational fluid dynamics to predictive analytical model. Langmuir 24, 10107–10115.

van Doormal, J.P., Raithby, G.D., 1984. Enhancement of the SIMPLEC method for predicting incompressible fluid flows. Numer. Heat Transfer Part B 7, 147–163.

Vladisavljević, G.T., Kobayashi, I., Nakajima, M., 2006. Production of monodisperse oil-in-water emulsions at high production scales using asymmetric microchannels. 7th Annual Meeting of Japan Society for Food Engineering, 2P2F-09.

Xu, J.H., Li, S.W., Wang, Y.J., Luo, G.S., 2006. Controllable preparation of monodisperse O/W and W/O emulsions in the same microfluidic devices. Langmuir 22, 7943–7946.

Xu, S., Nie, Z., Seo, M., Lewis, P.C., Kumacheva, E., Garstecki, P., Weibel, D., Gitlin, I., Whitesides, G.M., Stone, H.A., 2005. Generation of monodisperse particles using microfluidics: control over size, shape and composition. Angew. Chemie. Intnl. Ed. 44, 724–728.

Xu, Q., Nakajima, M., 2004. The generation of highly monodisperse droplets through the breakup of hydrodynamically focused microthread in a microfluidic device. Appl. Phys. Lett. 83, 3726–3728.

Yang, H., Bayyuk, S., Krishnan, A., Przekwas, A., Nguyen, L., Fine, P.

Yi, G.-R., Thorsen, T., Manoharan, V.N., Hwang, M.-J., Jeon, S.-J., Pine, D.J., Quake, S.R., Yang, S.-Y., 2003b. Generation of uniform colloidal assembles in soft microfluidic devices. Adv. Mater. 15, 1300–1304.

Yobas, L., Martens, S., Ong, W.-L., Ranganathan, N., 2006. High-performance flow-focusing geometry for spontaneous generation of monodispersed droplets. Lab Chip 6, 1073–1079.

Youngs, D.L., 1982. Time dependent multi-material flow with large fluid distortion. In: Morton KW, Banies MJ (eds) Numerical Methods for Fluid Dynamics, Academic Press, New York, pp. 273–285.

Zhou, C., Yue, P., Feng, J.J., 2006. Formation of simple and compound drops in microfluidic devices. Phys. Fluid 18, 092105.

Figure captions

Fig. 1. MC emulsification using asymmetric straight flow-through MCs (Kobayashi et al. 2010b). (a) Scanning electron micrograph of asymmetric straight flow-through MCs microfabricated within a 10×10 mm central region on a 24×24 mm silicon-on-insulator chip. (b) Example of the mass production of uniform soybean oil droplets from the slot outlets at a dispersed-phase flux of 100 L m^{-2} h^{-1}. A Milli-Q water solution containing 0.3 wt% sodium dodecyl sulfate was used as the continuous phase.

Fig. 2. Three-dimensional drawing of the geometry including a single asymmetric straight flow-through MC, used in the computational problem of this study.

Fig. 3. Structured grid generated in the computational domain and boundary conditions of the computational domain. (a) x-y plane ($z = 0$). (b) y-z plane ($x = 0$). (c) x-z plane ($y = 0$).

Fig. 4. Typical CFD simulation result of successful droplet generation via an asymmetric straight flow-through MC (t_{det} is the detachment time).

Fig. 5. CFD simulation result for velocity fields during droplet generation via an asymmetric straight flow-through MC. The velocity (U) of the liquids is positive when a liquid flows from bottom to top (t_{det} is the detachment time).

Fig. 6. Variation of droplet diameter (d_{drop}) and droplet generation rate (f) as a function of dispersed-phase velocity (U_d). Here, γ is the interfacial tension between the two phases. The experimental data of Vladisavljević et al. (2006) were used for comparison with the CFD results. Sauter mean diameter ($d_{3,2}$) measured with a light scattering instrument was used as

d_{drop} for the experimental results.

Fig. 7. (a) Three-dimensional snapshot of the oil-water interface during the detachment process. Here, $\Delta P_{d,MC}$ is the internal pressure of the dispersed phase at the channel outlet, $\Delta P_{d,slot,in}$ is the internal pressure of the dispersed phase in the slot, and $\Delta P_{d,slot,over}$ is the internal pressure over the slot. (b) Variation of $\Delta P_{d,MC}$, $\Delta P_{d,slot,in}$, and $\Delta P_{d,slot,over}$ as a function of detachment time (t_{det}).

Fig. 8. Variation of dimensionless droplet diameter ($\bar{d}_{drop}$) obtained from the CFD simulations as a function of dispersed-phase velocity (U_d); effect of channel size. Here d_{MC} is the channel diameter and Ca_d is the Capillary number of the dispersed phase that flows in a channel.

Fig. 9. (a) Schematic drawing of the main forces acting on a dispersed-phase droplet that expands over the slot outlet. Here, F_B is the buoyancy force, F_V is the viscous force, F_I is the inertial force exerted by a dispersed phase flowing out from an MC, and F_γ is the interfacial tension force. (b) Variation of F_B, F_V, F_I, and F_γ with channel diameter (d_{MC}). (c) Variation of the force ratio (($F_B + F_V + F_I$) / F_γ) with d_{MC}.

Fig. 10. (a) Variation of the droplet generation rate (f) with dispersed-phase velocity (U_d). (b) Variation of the maximum droplet generation rate (f_{max}) with d_{MC}.